

Micro-mechanical Failure Analysis of Wet Granular Matter

Konstantin Melnikov¹ · Falk K. Wittel¹ · Hans J. Herrmann¹.

Received: date / Accepted: date

Abstract We employ a novel fluid-particle model to study the shearing behavior of granular soils under different saturation levels, ranging from the dry material via the capillary bridge regime to higher saturation levels with percolating clusters. The full complexity of possible liquid morphologies [22] is taken into account, implying the formation of isolated arbitrary-sized liquid clusters with individual Laplace pressures that evolve by liquid exchange via films on the grain surface [15]. Liquid clusters can grow in size, shrink, merge and split, depending on local conditions, changes of accessible liquid and the pore space morphology determined by the granular phase. This phase is represented by a discrete particle model based on Contact Dynamics [3], where capillary forces exerted from a liquid phase add to the motion of spherical particles. We study the macroscopic response of the system due to an external compression force at various liquid contents with the help of triaxial shear tests. Additionally, the change in liquid cluster distributions during the compression due to the deformation of the pore space is evaluated close to the critical load.

Keywords Wet granular material · Triaxial shear test · Contact dynamics · Shear strength · Liquid clusters

1 Introduction

The presence of liquid is known to have a significant impact on the mechanical properties of granular mate-

rials [9, 16]. An illustrative example we know from our childhood are sand castles: while it is nearly impossible to build with dry sand, one can easily accomplish this task after mixing some water to it. However, if we keep on adding more water, from a certain saturation on, the structures collapse. Cohesion by capillary forces is the reason for the change in material behavior. After reaching a maximum at lower saturation [22], cohesive forces slowly decrease until the gravitational load gets too large. The nature of this phenomenon can be studied by tracking the liquid distribution on the micro-scale. In the last years, advanced experimental tools like micro-tomography created this possibility and Scheel *et al.* found a rich variety of liquid cluster morphologies [21, 22] beyond the well-studied liquid bridge regime [11, 12, 19, 24]. The number and the size of observed liquid clusters proved to strongly depend on the saturation level. Inspired by these findings, we developed a model that explicitly takes into account all possible liquid morphologies on the pore scale inside a random sphere packing [15]. Better understanding of the impact of higher liquid content is crucial for solving a number of open problems including e.g. rainfall-induced slope failures or fluid motion in sheared granular systems.

Wet granulates at low saturation, i.e. being in the so-called pendular state, are well studied [7, 11, 19, 23, 24]. With regard to cohesion the fully saturated state resembles the dry one since all cohesive forces vanish. However intermediate states, as well as the evolution of liquid structures under imbibition and drainage are rarely addressed due to their complexity. Starting from our grain-scale model for arbitrary saturation [15], we now allow particles to move and introduce a coupling between fluid and particles. Our intention is to investigate the effect of higher saturation on the macroscopic behavior of the material and vice versa the effect of

Konstantin Melnikov

¹Computational Physics for Engineering Materials,
ETH Zurich, Stefano-Franscini-Platz 3, CH-8093 Zurich,
Switzerland

E-mail: konstantin.melnikov@ifb.baug.ethz.ch

macroscopic deformations on the morphogenesis of the liquid body. To capture the effect of hydrostatic stress, triaxial shear tests are simulated at different initial saturation states [1, 25].

First we give a short description of the model with respect to the used discrete particle method (DPM) of contact dynamics (CD), before we summarize the most important features of the implemented liquid structure and evolution model. Special attention is given to the coupling between fluid and particles. The numerical procedure is described in detail and the triaxial shear cell used for measuring macroscopic behavior is introduced. We discuss the macroscopic response of the granular material to external compression for different saturation levels and the respective observations of the liquid body before we summarize main results and draw conclusions in Sec. 4.

2 Fluid-Particle Model for Arbitrary Liquid Saturation

We focus on wet granular material at various saturation levels under triaxial compression. Consequently one has to consider a solid, liquid and gaseous phase in the model. We limit ourselves to granular material consisting of uni-sized spherical particles and simulate time evolution of the dense packing under external load by Contact Dynamics. For the liquid phase, we develop a grain-scale model, capable of resolving the liquid body by combinations of capillary bridges, menisci and fully saturated pores. This way we resolve local liquid clusters from the dry to the fully saturated state. However gas can be trapped inside of pores, that is considered as incompressible.

2.1 Solid Phase Model

The solid phase is modeled using a DPM based on Contact Dynamics (CD). Originally proposed by Moreau [17, 3], this method is particularly suited representing rigid frictional particle systems with high packing fractions but negligible particle elasticity. Hence Newton's equations of motion are integrated implicitly, considering a volume exclusion constraint to avoid overlap of particles. In such systems, the rearrangements of rigid, frictional particles exclusively determines the system's behavior.

Each particle experiences a force \mathbf{F}_p that is composed of the contact forces \mathbf{F}_c with all contacting particles and the wall, a gravitational force \mathbf{F}_{ext} , as well as forces from the liquid, that are described along with the considered liquid structures in Sec. 2.2.1. The essential

difference between CD and soft particle methods is the strict volume exclusion constraint, where the normal force component F_n can take arbitrary large positive values if the distance or gap $s_{ij} = 0$ between surfaces of particle i and j , to prevent interpenetration of surfaces (see Fig.1). Hence, in an iterative process the position of the particle must be found for which the normal force component \mathbf{F}_n of each active contact is minimal for all active contacts such that there is no overlap of particles at the next time step. When $s_{ij} > 0$, the corresponding F_n vanishes, unless attractive cohesive forces $-F_{coh}$ act in the normal direction, e.g. in a range $0 < s_{ij} < s_{int}$. Sliding between particles is prevented if the tangential component of the contact force F_t does not exceed the threshold given by the Coulomb friction coefficient μ : $0 \leq F_t \leq \mu F_n$ (see Fig. 1(b)). Note that the static friction coefficient is set equal to the dynamic one. The tangential force at the contact point and the resulting moment around the particle center lead to particle rotation.

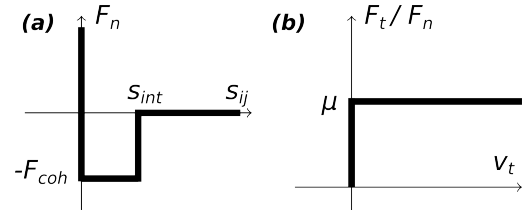


Fig. 1 Contact laws in Contact Dynamics. (a) Repulsive normal force F_n with volume exclusion constraint for $s_{ij} = 0$ and attractive cohesive force F_{coh} with interaction distance s_{int} . (b) Sliding of particles is suppressed until the tangential force F_t is smaller than the Coulomb friction threshold μF_n .

In a dense packing, many particles are interacting in a force contact network. The contact forces acting on each particle are influenced by adjacent contact forces in the neighborhood, requiring a global solution of contact forces. The ones for a particle are described by a system of equations which can be approximately solved by an iterative algorithm on all particles in a random order. Over several iterations, the global contact force network relaxes towards a state where only minor changes occur. The calculated forces are then used to integrate the equations of motion by an implicit Euler method. The larger computational cost for the iterative force calculation is often outbalanced in CD by the possibility to use significantly larger time steps compared to soft particle dynamics.

2.2 Liquid Phase Model

From micro tomography experiments it is known, that liquid builds highly complex structures inside the granular material above the liquid bridge regime [22]. In order to simulate this behavior, we use a general model for liquid saturation which is able of resolving all possible liquid structures observed in experiments. In this section we give a short overview of this model, while the detailed description can be found in Ref. [15].

Based on the exact geometrical positions of the particles, the pore-throat network is constructed via Delaunay triangulation. The void space in each tetrahedral cell of the triangulation (see Fig. 2(c)) is called the pore body, while the cutting areas of the pore body with the respective faces of the cell form the four pore throats. Liquid clusters are represented as a combination of three types of elementary units: **liquid bridges**, **menisci** and entirely filled **pore bodies**. These elements can form higher geometrical configurations called **liquid clusters**. This evolution is determined by local instability criteria for imbibition and drainage.

2.2.1 Basic Liquid Structures

The elemental liquid structure involving two grains i and j of radius R , is a **liquid bridge** (Fig. 2(a)). With their centers P_i, P_j and R , the inter-particle separation distance S_{ij} is given. In general, the pressure drop $\Delta P = P_{liquid} - P_{gas}$ across the liquid-gas interface with surface tension γ and curvature $C = 1/R_1 + 1/R_2$ with the principal radii of curvature $R_{i,j}$, is described by the Young-Laplace equation [5]: $\Delta P = \gamma C$. We interpolate the solution of this equation for liquid bridges from tabulated values by Semprebon *et al.* [13] obtained with a numerical energy minimization method (NEM) of the software Surface Evolver [2] for a constant contact angle $\theta = 5^\circ$. With the liquid volume of the bridge V_{ij} , being a state variable, we interpolate $\Delta P_{ij}(R_i/R_j, V_{ij}, S_{ij})$, as well as the filling angle $\beta_{ij}(R_i/R_j, V_{ij}, S_{ij})$ from the tables. The capillary force of the liquid bridge \mathbf{F}_{ij} acting on particles i and j in the direction given by the unit vector \mathbf{e}_{ij} from P_i to P_j is calculated via the experimentally found expression by Willett *et al.* [26]

$$\mathbf{F}_{ij} = -\mathbf{F}_{ji} = \mathbf{e}_{ij} \cdot \frac{2\pi R \gamma \cos \theta}{1 + 0.5 S_{ij} \sqrt{R/V_{ij}} + 2.5 S_{ij}^2 R/V_{ij}}. \quad (1)$$

Note that for contact ($S_{ij} = 0$) the capillary force is independent of V_{ij} , resulting in a constant force $|F_{ij}|$, provided $\gamma = const$ and $\theta = const$.

As soon as three particles i, j, k with respective liquid bridges lb_{ij}, lb_{ik} and lb_{jk} are involved, the remaining pore throat can be filled, on condition that enough

liquid is stored in the bridges, resulting in trimer formation (Fig. 2(b)). Based on ideas by Haines [8], we model the resulting liquid body of equal Laplace pressure by adding to the three bridges a fluid filled cylindrical pore throat that is located between the grains and limited by two **menisci** of spherical shape as liquid-gas interface (see section cut Fig. 3). The position of the meniscus center O and its radius R_{men} is calculated following the geometric construction proposed by Gladkikh [6] with contact angle θ . O and R_{men} determine the fluid volume in the cylindrical pore throat V_{cyl} of radius R_{cyl} and height H_{mem} . C_i denotes the contact point between meniscus and particle i (see Figs. 2(b), 3). The negative pressure drop ΔP across the meniscus is calculated using the Young-Laplace equation with the constant curvature $C = 1/R_{men}$. A capillary force $\mathbf{F}_{i,j,k}$ from the meniscus acts on particles i, j, k additionally to the forces from the liquid bridges. For simplicity, it acts in the direction given by the points $\overline{P_i T}$ (see Fig. 3) with the unit vector \mathbf{e}_{iT} and is calculated as $\mathbf{F}_{i,j,k} = \mathbf{e}_{iT} \cdot \Delta P A_{eff}$ with the effective wetted area A_{eff} defined for example for particle i by a triangle through the points $C_i - A_{i1} - A_{i2}$ (in Fig. 2).

With four particles, a tetrahedral cell can be formed, with the void space in the center being filled by a **pore body**. This pore body can be either connected to another filled pore body or it can be bounded by a meniscus through each of the four existing pore throats. In the latter case, the meniscus defines the Laplace pressure of the liquid phase inside the pore. The Laplace pressure drop ΔP leads to a capillary force component due to the wetted particle surface area inside the pore body. The resulting capillary force \mathbf{F}_{cap} pulls each of the four particles towards the center of the pore as shown in Fig. 2(c). The respective wetted particle surface area is the surface of each particle inside the triangulation cell. If a liquid bridge between the corresponding particles exists, their wetted area is reduced in the calculation by the wetted area of the liquid bridge with opening angle β_{ij} . Note that in this case we do not correct the direction of the force and for simplicity keep it directed from the particle to the cell center. When particles are entirely immersed in liquid, forces from the pore body vanish, since the pressure inside the cluster is constant. When a tetrahedral cell contains four menisci, an incompressible gas bubble can be trapped.

The elementary units liquid bridge, meniscus, and filled pore body are the building blocks of local **liquid clusters** which can evolve inside the granular material (see Fig. 2(1-2)). Following the description of Scheel *et al.* [22] for clusters without filled pore bodies, we call the smallest possible cluster trimer (three contacts, see Fig. 2b), the next one is a pentamer, heptamer and

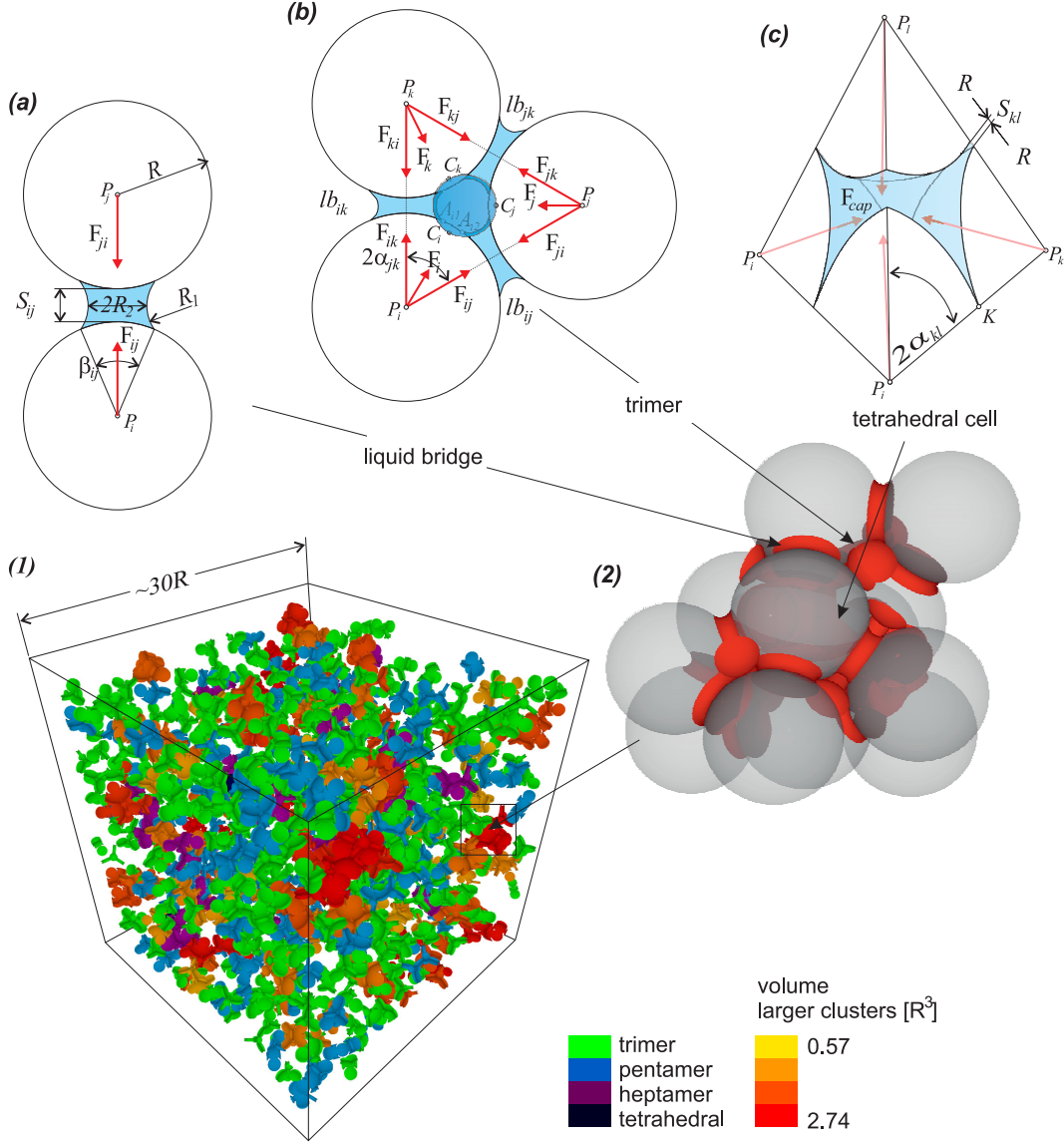


Fig. 2 (Color online) Liquid clusters emerging in a sphere packing at liquid content $W_c = 3\%$ (1) and one exemplary cluster (2), composed of three basic liquid structures: bridges (a), trimers (b), and tetrahedral cell (c) with definitions given in the text. Note that in (b), C_i is located above the trimer plane.

if more than 7 contacts are involved we simply call it cluster. The smallest cluster with a filled pore body is a tetrahedral cluster consisting of 6 associated liquid bridges and 4 menisci. We assume that pressure inside a each liquid cluster is constant, implying that all menisci have the same curvature. Pressure is calculated individually for each liquid cluster based on its volume [15], which is the control variable of the model. With N_{imb} imbibed pore bodies and N_{men} menisci in a cluster

$$V_c(R_{men}) = \sum_{i=0}^{N_{imb}} V_{pore,i} + \sum_{j=0}^{N_{men}} V_{men,j}(R_{men}), \quad (2)$$

where $V_{pore,i}$ denotes the volume of the imbibed pore body i and $V_{men,j}$ the volume of the meniscus j including its associated liquid bridges. The volume of the filled pore is calculated by subtracting the partial volumes of the four particles contained within the tetrahedral cell from the volume of this cell. The second component in the term $V_{men}(R_{men})$ accounts for the volumes of the liquid bridges V_i^{lb} associated with the meniscus i :

$$V_{men}(R_{men}) = V_{cyl}(R_{men}) + (0.5 + \varepsilon) \sum_{i=0}^m V_i^{lb}(R_{men}). \quad (3)$$

The geometrical correction parameter ε describes the volume excess of a real meniscus with the connected liquid bridges, compared to our approximation in which

V_{cyl} underestimates the volume bounded by the meniscus (see Fig. 3 red area and Ref. [15]). Only half of each bridge volume is considered in the above formula since the other half is located in the opposite triangulation cell.

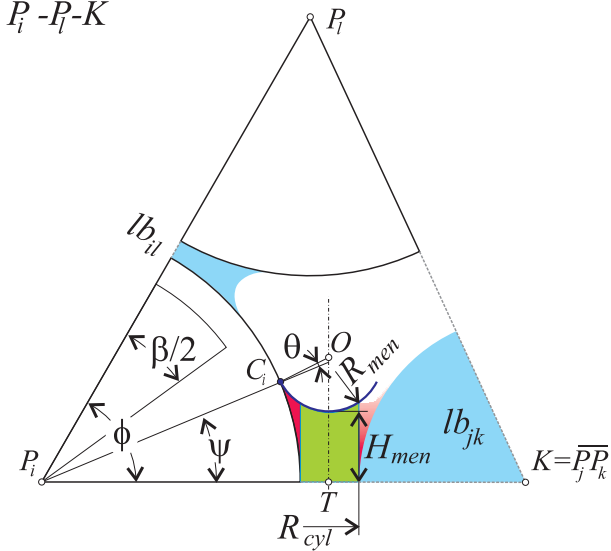


Fig. 3 Sectional view of tetrahedral cell through P_i - P_l - K (Fig. 2) showing the meniscus position in the pore throat. Point O defines the center of the spherical cap shaped meniscus of radius R_{men} . The green area below approximates the meniscus volume by a cylinder of radius R_{cyl} and height H_{men} , while the red area points at the underestimated volume.

2.2.2 Evolution of Liquid Structures

Liquid structures can change due to relative particle movements or volume changes, for example through condensation or evaporation at gas-liquid interfaces or by local liquid sources or sinks. To take recent experimental observations into account [10, 22], we include transport via the liquid film on the particle surface. This transport occurs at low and intermediate saturations, where liquid exists in form of spatially disconnected clusters. For stationary flow in the film, the volume flux \dot{V}_i into structure i is proportional to the local Laplace pressure differences between liquid structures sharing at least one grain. If N_i structures can be connected to the same grain, one obtains

$$\dot{V}_i = \frac{R}{\gamma} \cdot \sum_{j=0}^{N_i} \omega_{ij} (P_j - P_i), \quad (4)$$

with the dimensionless conductance coefficient ω_{ij} that defines the equilibration time scale. In general ω_{ij} should depend on details like distance between structures, the

number of structures connected to the grain and others [13, 14]. However for simplicity we set $\omega_{ij} = 0.01$ for all presented simulations (see Tab. 1). Particle movement, as well as flow from or into liquid structures can trigger local instabilities that propagate liquid interfaces inside the porous particle packing. This is consequently a discontinuous process with instantaneous jumps between stable configurations. Micro mechanically, these interface jumps are associated with drainage or imbibition of pore bodies or throats, or bridge rupture. We identified a set of seven geometrical criteria for instability, similar to Motealleh *et al.* [18] and Gladkikh [6], with criteria **i1-i4** for imbibition and **d1-d3** for drainage:

Criterion i1: If two liquid bridges with filling angles $\beta_{ij,ik}$ touch each other, they can form a new trimer by filling the pore throat if sufficient liquid for a stable meniscus according to the drainage criterion **d1** is available. With the opening angle α_{jk} (see Fig. 2(b)) it reads $0.5(\beta_{ij} + \beta_{ik}) > 2\alpha_{jk}$.

Criterion i2: If a meniscus in a tetrahedral cell touches a single liquid bridge, that was up to now not part of the liquid body, the pore body is filled. Hence the respective meniscus with the filling angle of the meniscus ψ and the face-edge angle ϕ shown in Fig. 3 becomes unstable when $\psi + \beta/2 > \phi$.

Criterion i3: If the centers of two menisci O inside one pore body touch, they build a single spherical interface and can fill the pore body (see Fig. 3), however with all four menisci formed, a gas bubble gets trapped.

Criterion i4: If a meniscus touches the opposite particle, the pore body is imbibed.

Criterion d1: Pore throats will drain if they reach a minimum size, expressed by the critical height of the menisci $H_{men}^{min} \geq \kappa R$ with the arbitrary drainage parameter κ . Best agreement with experimental data was found for $\kappa = 0.15$ [15].

Criterion d2: Pore bodies become unstable when the center of the meniscus of a neighboring cell touches the respective pore throat plane of an entirely saturated cell. Instantaneously the liquid interface jumps to a new stable position, leaving behind a drained pore body.

Criterion d3: Liquid bridges between particles i and j can rupture when the empirical expression derived by Willett *et al.* [26] for the rupture distance $S_c \simeq (1 + \frac{1}{2}\theta)(\sqrt[3]{V_{ij}} + \sqrt[3]{V_{ij}^2}/10)$ in units of the particle radius R to the bridge volume V_{ij} is reached (see Fig. 2(a)). S_c in combination with a zero distance for the formation of liquid bridges results in the hysteretic behavior of wet granular material. V_{ij} is sucked back to the surface of the holding particles and redistributed equally to their other contacts [12].

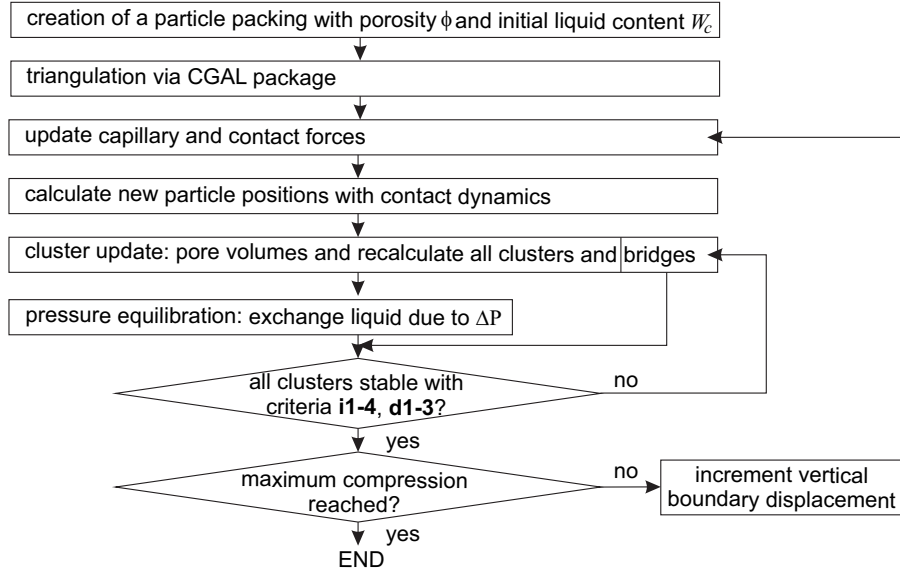


Fig. 4 Simulation scheme.

2.3 Numerical Procedure

The different steps of the numerical procedure are schematized in Fig. 4, while a detailed description of the system construction and fluid calculation was previously published in Melnikov *et al.* [15]. The initial packing, that is dynamically created via the DPM model (see Sec. 2.1) already allows for the introduction of an initial liquid content by assigning a liquid film to each particle, small enough to stay in the pendular regime [9]. When particles contact, liquid bridges are created that can rupture under criterion **d3**. We define the liquid content W_c as total liquid volume V_{liquid} normalized by the void volume V_{void} : $W_c = V_{liquid}/V_{void}$, where the void volume V_{void} is calculated as the difference between the sample volume V_{sample} and the total volume of the grains V_{grains} . The porosity ϕ is defined as $\phi = 1 - \phi_s$, where ϕ_s is the solid fraction given by the total volume of N_p particles via $\phi_s = 4N_p\pi R^3/(3V_{sample})$. Before entering the simulation, the pore space is triangulated into tetrahedral cells using a Delaunay triangulation on particle centers [4]. To increase W_c , liquid is condensed into already existing bridges, leading to formation of local clusters due to occurring instabilities. To avoid boundary effects with the wall, we suppress the formation of liquid structures at a distance $d \approx 2R$ from all walls. After addition of liquid to existing structures, we recalculate them such that the Laplace pressure corresponds to the changed volume. Before checking for instabilities, the liquid transport due to Laplace pressure gradients is calculated for the entire time increment, leading to equilibration of pressure differences. Then the instability criteria for imbibition **i1-i4** and drainage **d1-d3** are

checked in ascending order. Identified instabilities are eliminated through drainage or imbibition as described in Sec. 2.2.2 and a cluster update is made before the time is incremented by Δt . During the new time step, we first update particle positions through the DPM algorithm, and consecutively calculate the respective liquid body configuration as described above. To ensure conservation of the total liquid volume in the specimen, all liquid clusters are subsequently recalculated considering the changed volume of the pore bodies. Note, that in this paper we stick to small strains up to 4% to be able to retain the initial pore-throat network.

2.4 Triaxial Shear Test Model

To study the shear strength of the wet granulate, we simulate triaxial shear tests that are a common tool in geotechnique for obtaining macroscopic systems responses [1, 24]. The cubic sample contains N_p randomly distributed particles of mass density ρ_p , radius R and hence particle mass m_p . To randomize the particles, the solid fraction is kept low, and random velocities are assigned to the particles, before the sample is confined by a hydrostatic pressure on each cube walls of mass $2000m_p$. To obtain the desired solid fraction $\phi_s = 0.6$, friction is omitted, resulting in initial system dimensions of $L_{x,0} = L_{y,0} = L_{z,0} \approx 32R$ (see Fig. 5). Note that in CD overlaps are avoided. Hence no elastic energy is stored in overlaps, opposite to soft particle dynamics. The confining forces on each wall F_{conf} are calculated with the respective stress $\sigma_{1,3}$ and the true area of the wall A_{wall} involved. σ_1 and σ_3 denote the confining pressures at the upper and side walls, respectively

(see Fig. 5). For the compression with $\sigma_1 \neq \sigma_3$ friction is switched on, and the mass of the bottom wall is set to infinity. The hydrostatic stress σ_3 is applied on all movable walls before the upper wall of the cubic sample is lowered at a constant strain rate $\dot{\nu} = v_w/L_z$ with the vertical displacement rate v_w . The strain rate $\dot{\nu}$ is chosen such that the assumption of quasi-static compression is satisfied, meaning that the response of the system for even lower strain rates would be the same. The unit of time T is defined as $T = 1/\dot{\nu}$ meaning that for a simulation with $\dot{\nu} = 0.0001 [1/T]$ the upper wall moves by a distance of $0.0001L_z$ during a time unit.

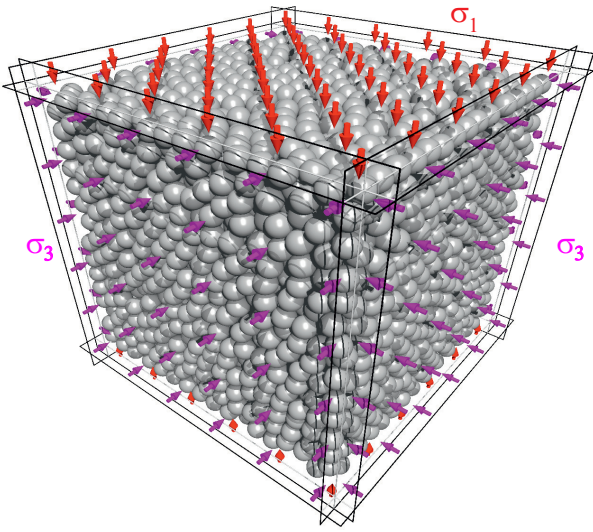


Fig. 5 Setup of the triaxial shear test with confining walls.

We calculate the differential stress $q = \sigma_1 - \sigma_3$ by measuring the normal stresses on the upper and the side walls from the reaction forces of the particle contacts. The axial strain is calculated via $\varepsilon_A = |L_z - L_{z,0}| / L_{z,0}$. Note, that we use the absolute value in the above definition which implies that the axial strain during compression is positive. The volumetric strain ε_V is calculated as $\varepsilon_V = \Delta V / V_0$ where ΔV is the volume change of the sample with respect to the initial volume V_0 .

3 Results of Wet Triaxial Shear Tests

To quantify the effect of liquid on the behavior of granular material under load, triaxial compression tests were simulated with increasing initial liquid content W_c from dry (0%) up to 40% and at three distinct values of confining pressure is $\sigma_3 = 20, 40, 60$ with the unit $u_p = m_p / (T^2 R)$. Since no dimensional quantities are used in Contact Dynamics, a direct comparison with experimental data can be done by considering the ratio of

Table 1 Parameters of the solid and liquid phase model.

Solid phase:		
N_p	5000	number of particles
R	1	particle radius
ρ_p	1	particle mass density
ϕ_s	0.60	solid fraction
Δt	0.001 - 0.01	time step
θ	5°	contact angle
μ	0.3	friction coefficient
Liquid phase:		
ω	0.01	conductance coefficient
ε	0.07	geometrical correction parameter
κ	0.15	drainage parameter for meniscus
γ	1	surface tension

inertial to confining forces proposed by Rognon *et al.* [20]: $I = \dot{\nu} R \sqrt{\rho_p / P}$ where $P = \sigma_3$ is the confining pressure. In our simulations this number is equal to $I_{20} \approx 2.2 \cdot 10^{-5}$, $I_{40} \approx 1.6 \cdot 10^{-5}$ and $I_{60} \approx 1.3 \cdot 10^{-5}$. Note, that these inertial numbers correspond to the quasi-static regime since our simulations show no changes if the strain rate $\dot{\nu}$ is further reduced. The resolution of local liquid structures gives the opportunity to study the evolution of liquid clusters during compression. We are interested in micro-mechanical changes in terms of morphology distributions of the liquid body or morphogenesis of individual clusters due to deformation. Finally we quantify the dependence of macroscopic dilatation and limit surfaces upon the liquid content.

3.1 Liquid Cluster Evolution During Compression

In particulate systems, shear typically results in dilatation, that can strongly effect the stability of the liquid body. For a sample with liquid content $W_c = 6\%$ and confining pressure of $\sigma_3 = 40u_p$ we analyze the consequences of the compression on the distribution of liquid cluster morphologies from the single bridge up to large clusters. In Fig. 6 the relative change of the number of liquid cluster morphologies N/N_0 with respect to the stress-free state at $t = 0$ (Fig. 2(1)) is given as function of the axial strain up to $\varepsilon_A = 4\%$. The compression in one axial direction as considered in this study leads to the dilatation of the sample in directions perpendicular to this axis. A drop in solid fraction and increasing sample volume are the consequences. Since dilatation means increasing inter-particle distances, it is not surprising that isolated liquid bridges become less common with increasing strain due to bridge rupture. The liquid is used for the formation of new trimers and of other cluster morphologies like pentamers and large clusters. Because of the limited sample size with $N = 5000$, the total number of larger cluster morphologies is consequently small, resulting in strong fluctuations for tetra-

hedral clusters and heptamers. Nevertheless, one can conclude that the pore space deformation triggers new instabilities that lead to trimer formation and consolidation of existing clusters into larger structures. This process is fueled by the liquid volume from existing liquid bridges as their number drops and from other existing structures by coalescence.

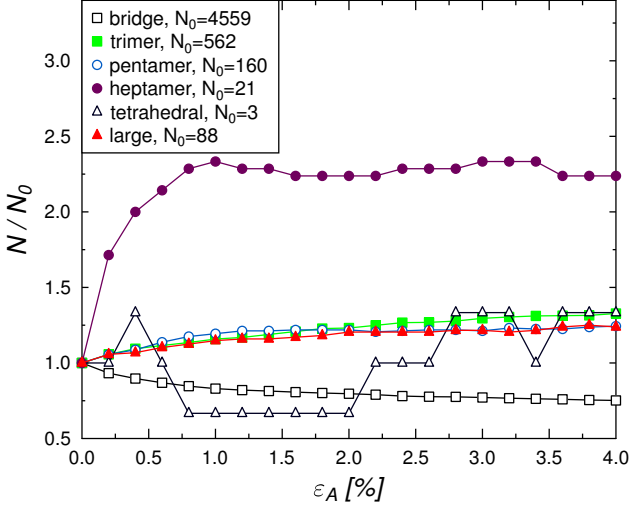


Fig. 6 Evolution of the liquid cluster morphologies N scaled by N_0 at $t = 0$ as a function of the axial strain ε_A . Liquid content $W_c = 6\%$, normal stress on the vertical walls $\sigma_3 = 40u_p$.

The deformation does not only have an effect on the statistics of liquid clusters. In particular for large deformations, parameters that characterize the cluster morphology evolve. We exemplify the morphogenesis of a single liquid cluster during the triaxial shear test ($W_c = 22\%$; $\sigma_3 = 40u_p$). While it remains rather isochoric with $V \approx 100R^3$, there are changes in the number of individual units which constitute the cluster as the axial strain ε_A increases (see Fig. 7). This is observed for the number of individual units like menisci, liquid bridges and filled pore bodies (see Sec. 2.2.1). The axial compression leads to spreading of the cluster in the plane vertical to the axial load, which can be seen from the increasing number of menisci. The increasing number of menisci can be explained by the formation of new trimer units due to local instabilities or the incorporation of already existing trimers by the large cluster after contacting. Note, that although we take a look at a single cluster here, also other (smaller) clusters exist in the sample. The number of filled pore bodies and the number of liquid bridges decrease after reaching a local maximum due to increasing inter-particle distances from dilatation in σ_3 directions that resulted in liquid bridge ruptures. The cluster evolves from a

compact shape into a looser structure. The rapid increase of the number of menisci and filled pore bodies in the beginning (small strains ε_A) does not result in a higher cluster volume because the Laplace pressure decreases when new pores are filled. A lower Laplace pressure leads to a decrease of menisci volumes since they move deeper into pore throats, see Fig. 3.

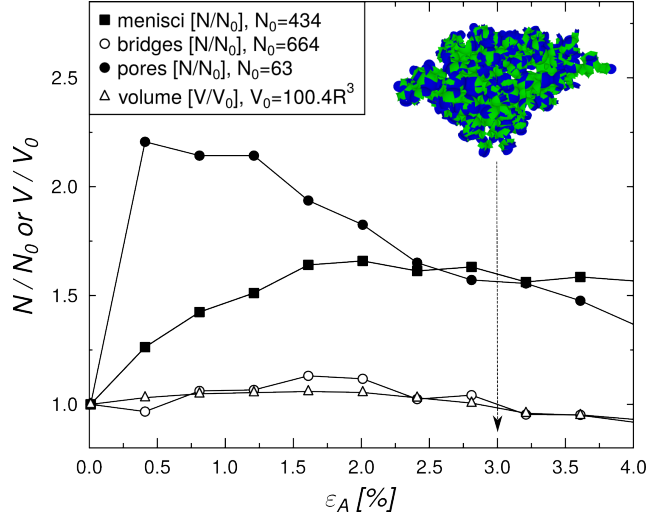


Fig. 7 Development of characteristic properties describing a single cluster as a function of the axial strain ε_A : volume of the cluster, menisci, bridges and filled pore bodies. Inset: liquid body of the studied cluster at $\varepsilon_A = 3\%$. Bridges are colored blue and menisci are green.

3.2 Dependence of Limit Surfaces on Liquid Content

We previously referred to the role of the volumetric strain ε_V . Its dependence on the axial strain ε_A and confining pressure σ_3 is shown in Fig. 8. We observe a decrease of ε_V with increasing σ_3 , similar to Ref. [23]. A typical observation is that the spread between volumetric strain curves for different confining pressures increases with increasing axial strain. Note that the spontaneous increase of $q = \sigma_1 - \sigma_3$ is a consequence of the Contact Dynamics approach. Comparable studies with the soft particle contact models exhibit a slight initial decrease of the sample volume due to the elasticity of the particles (see e.g. Ref [24]). Attractive capillary forces hinder the spatial rearrangement of particles, resulting in a slightly higher volumetric strain for the wet sample (see Fig. 8).

During the compression, the differential stress $q = \sigma_1 - \sigma_3 [u_p]$ is calculated as function of the axial strain ε_A . In Fig. 9 the stress-strain curve exhibits a rapid increase for small ε_A independent on the liquid content W_c . This behavior is typical for a dense packing

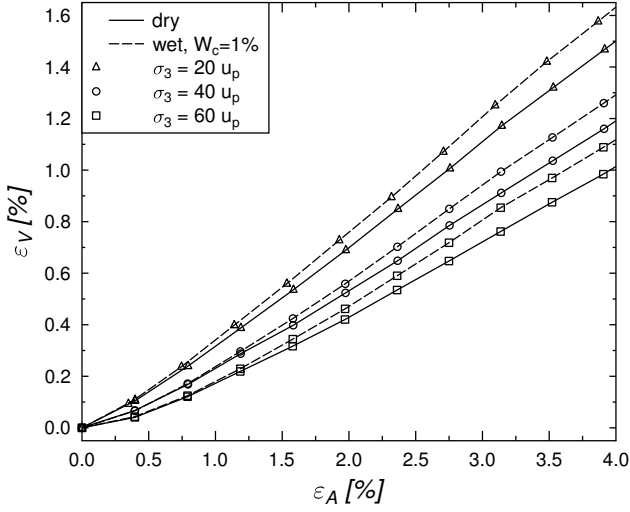


Fig. 8 Volumetric strain ε_V as a function of axial strain ε_A for different confining pressures σ_3 .

and in agreement with experimental [25] and numerical observations [1, 23]. For larger strains, q saturates and reaches a constant plateau, whose value depends on W_c .

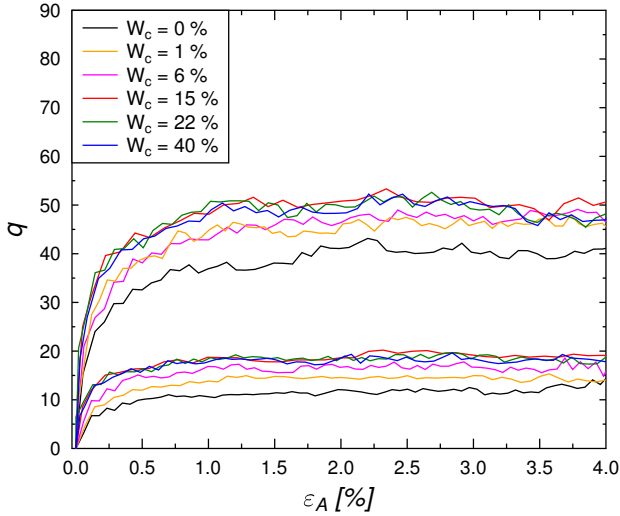


Fig. 9 Differential stress q versus axial strain ε_A for different liquid contents W_c . Two values of confining pressure σ_3 are considered: $\sigma_3 = 20u_p$ (plateau in the range $7u_p < q < 20u_p$) and $\sigma_3 = 60u_p$ (plateau in the range $35u_p < q < 55u_p$).

When monitoring the shear strength, or maximum in differential stress q_{max} as function of the liquid content W_c (see Fig. 9) at a single value of confining pressure, one can see a huge increase from the dry state to $W_c = 1\%$, corresponding to a pendular state where only liquid bridges exist. From there on, the gradient in shear strength with respect to liquid content

quickly decays. Our data suggests a maximum in shear strength between $15\% \leq W_c \leq 22\%$, followed by a decay that in principle should reach the one of the dry state for $W_c = 100\%$. Shear strength versus confining pressure can be approximated by a straight line which goes through zero for the dry granular material (see Fig. 10). This behavior is well known [24] and described by the Mohr-Coulomb failure criterion in the form

$$\tau = \mu_f \sigma + c, \quad (5)$$

where τ is the shear strength, $\mu_f = \tan(\psi)$ the internal friction coefficient, ψ denotes the angle of internal friction and c cohesion. The curves for wet material also show a linear trend, but with cohesion that results from the sum of capillary forces of all liquid bridges and clusters. When looking at the dependence of c on the liquid content W_c (see Fig. 10(inset)) it becomes evident that the increased shear strength is due to an increased cohesion and not to a change in ψ . As a matter of fact ψ proves to be independent on the liquid content within our statistical error bars at $\psi = 35.9^\circ$. The maximal increase in shear strength is about $5u_p$, independent on the confining pressures.

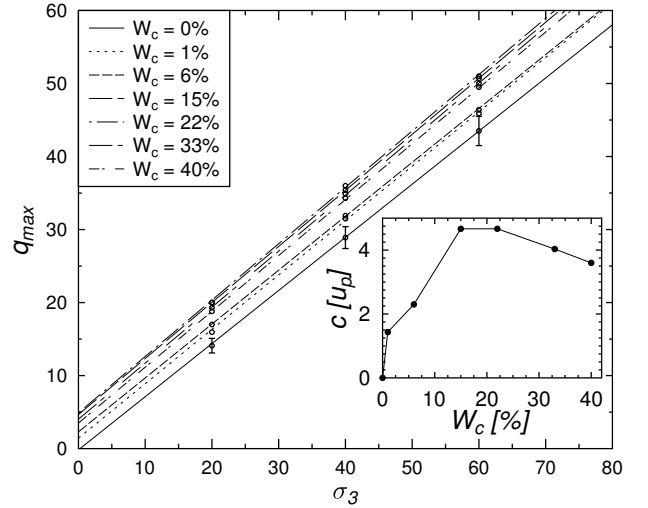


Fig. 10 Mohr-Coulomb failure envelope: maximal values of differential stress q_{max} as a function of confining pressure σ_3 . The data (single points) was extracted from the curves shown in Fig. 9 by taking an average between $1.5\% < \varepsilon_A < 3.5\%$. Straight lines are the fit curves to the single data points. Error bars for $W_c = 0\%$ exemplary visualize the uncertainty due to fluctuations of q_{max} in the numerical simulation which increase with σ_3 . Inset: Cohesion c as a function of liquid content W_c , extracted from the intersection of the lines with the q_{max} axis at $\sigma_3 = 0$.

4 Summary and Conclusions

The described micro-mechanical model couples liquid structures to individual moving particles. For simplicity, the solid phase consists of spherical particles whose evolution in time and space is simulated with Contact Dynamics. For the liquid phase, the model incorporates rather complicated liquid structures observed in experiments which became feasible due to recent advances in the micro-tomography technique [22]. To ensure the conservation of mass, volume is chosen as the control variable in the model. The corresponding pressure is calculated separately for each liquid structure. The fluid-particle coupling induces cohesive forces exerted by the liquid structures on the holding particles. Note, that the present version of the model is limited to small strains up to 4-5% where an initial triangulation structure does not need to be updated. For higher strains the particle positions must be triangulated anew to provide a valid pore network. The proposed model was applied for the simulation of triaxial compression tests at different saturation levels. We could qualitatively reproduce results reported in both numerical and experimental studies, including the well-known Mohr-Coulomb failure criterion. Furthermore, shear tests well beyond the pendular regime were simulated. Due to the micro-mechanical approach, we were able to track and characterize the evolution of liquid structures inside the deforming granular material and to relate it to the deformation state. In the future we will extend the model to larger deformations.

Acknowledgements The research leading to these results has received funding from the People Programme (Marie Curie Actions) of the European Union's Seventh Framework Programme FP7 under the MUMOLADE ITN project (Multi-scale Modelling of Landslides and Debris Flow) with REA grant agreement n° 289911, as well as from the European Research Council Advanced Grant no. 319968-FlowCCS and the DFG under PiKo SPP 1486 HE 2732/11-3.

References

1. Belheine N, Plassiard JP, Donzé FV, Darve F, Seridi A (2009) Numerical simulation of drained triaxial test using 3D discrete element modeling. *Computers and Geotechnics* 36(12):320–331, DOI 10.1016/j.compgeo.2008.02.003
2. Brakke K (1996) The surface evolver and the stability of liquid surfaces. *Phil Trans R Soc A* 354:2143–2157 DOI 10.1098/rsta.1996.0095
3. Brendel L, Unger T, Wolf DE (2005) *Contact Dynamics for Beginners*, Wiley-VCH Verlag, pp 325–343. DOI 10.1002/352760362X.ch14
4. Caroli M, Teillaud M (2015) {3D} Periodic Triangulations. In: {CGAL} User and Reference Manual, 4th edn, CGAL Editorial Board
5. de Gennes PG, Wyard FB, Quèrè D (2003) *Capillary and wetting phenomena: bubbles, pearls, waves*, Springer, pp 325–343
6. Gladkikh M (2005) *A Priori Prediction of Macroscopic Properties of Sedimentary Rocks Containing Two Immiscible Fluids*. PhD thesis, University of Texas at Austin
7. Gröger T, Tüzün U, Heyes DM (2003) Modelling and measuring of cohesion in wet granular materials. *Powder Technology* 133(13):203–215, DOI 10.1016/S0032-5910(03)00093-7
8. Haines WB (1927) Studies in the physical properties of soils: IV. A further contribution to the theory of capillary phenomena in soil. *The Journal of Agricultural Science* 17(02):264–290, DOI 10.1017/S0021859600018499
9. Herminghaus S (2005) Dynamics of wet granular matter. *Adv Phys* 54(3):221–261, DOI 10.1080/00018730500167855
10. Lukyanov AV, Sushchikh MM, Baines MJ, Theofanous TG (2012) Superfast Nonlinear Diffusion: Capillary Transport in Particulate Porous Media. *Phys Rev Lett* 109(21):214,501, DOI 10.1103/PhysRevLett.109.214501
11. Mani R, Kadau D, Or D, Herrmann HJ (2012) Fluid Depletion in Shear Bands. *Phys Rev Lett* 109(24):248,001, DOI 10.1103/PhysRevLett.109.248001
12. Mani R, Kadau D, Herrmann HJ (2013) Liquid migration in sheared unsaturated granular media. *Granular Matter* 15(4):447–454, DOI 10.1007/s10035-012-0387-3
13. Mani R, Semprebon C, Kadau D, Herrmann HJ, Brinkmann M, Herminghaus S (2015) Role of contact-angle hysteresis for fluid transport in wet granular matter. *Phys Rev E* 91(4):42,204, DOI 10.1103/PhysRevE.91.042204
14. Mani RA (2014) *Capillary interactions, shear thickening and liquid migration in wet granular media*. PhD thesis, ETH Zurich
15. Melnikov K, Mani R, Wittel FK, Thielmann M, Herrmann HJ (2015) Grain-scale modeling of arbitrary fluid saturation in random packings. *Phys Rev E* 92:022,206, DOI 10.1103/PhysRevE.92.022206
16. Mitarai N, Nori F (2006) Wet granular materials. *Adv Phys* 55(1-2):1–45, DOI 10.1080/00018730600626065
17. Moreau JJ (1994) *Some numerical methods in multibody dynamics: application to granular ma-*

- terials. *European journal of mechanics A Solids* 13:93–114
18. Motealleh S, Ashouripashaki M, DiCarlo D, Bryant S (2013) Unified Model of Drainage and Imbibition in 3D Fractionally Wet Porous Media. *Transport in Porous Media* 99(3):581–611, DOI 10.1007/s11242-013-0201-7
 19. Richefeu V, El Youssoufi MS, Radjaï F (2006) Shear strength properties of wet granular materials. *Phys Rev E* 73(5):51,304, DOI 10.1103/PhysRevE.73.051304
 20. Rognon PG, Roux JN, Wolf D, Naaïm M, Chevoir F (2006) Rheophysics of cohesive granular materials. *EPL (Europhysics Letters)* 74(4):644
 21. Scheel M (2009) Experimental investigations of the mechanical properties of wet granular matter. PhD thesis, Georg-August-Universitaet Goettingen
 22. Scheel M, Seemann R, Brinkmann M, Michiel MD, Sheppard A, Breidenbach B, Herminghaus S (2008) Morphological clues to wet granular pile stability. *Nat Mater* 7(3):189–193, DOI 10.1038/nmat2117
 23. Scholtès L, Chareyre B, Nicot F, Darve F (2009) Micromechanics of granular materials with capillary effects. *International Journal of Engineering Science* 47(11-12):1460–1471, DOI 10.1016/j.ijengsci.2009.10.003
 24. Scholtès L, Hicher PY, Nicot F, Chareyre B, Darve F (2009) On the capillary stress tensor in wet granular materials. *International Journal for Numerical and Analytical Methods in Geomechanics* 33(10):1289–1313, DOI 10.1002/nag.767
 25. Wang Q, Lade PV (2001) Shear Banding in True Triaxial Tests and Its Effect on Failure in Sand. *J Eng Mech* 127(8):754–761, DOI 10.1061/(ASCE)0733-9399(2001)127:8(754)
 26. Willett CD, Adams MJ, Johnson SA, Seville JPK (2000) Capillary Bridges between Two Spherical Bodies. *Langmuir* 16(24):9396–9405, DOI 10.1021/la000657y